

Terahertz chiral metamaterials with giant and dynamically tunable optical activity

Jiangfeng Zhou,^{1,*} Dibakar Roy Chowdhury,¹ Rongkuo Zhao,² Abul K. Azad,¹ Hou-Tong Chen,^{1,†} Costas M. Soukoulis,² Antoinette J. Taylor,¹ and John F. O'Hara^{1,‡}

¹Center for Integrated Nanotechnologies, Materials Physics and Applications Division, Los Alamos National Laboratory, Los Alamos, New Mexico 87545, USA

²Ames Laboratory and Department of Physics and Astronomy, Iowa State University, Ames, Iowa 50011, USA

(Received 20 February 2012; published 27 July 2012)

We demonstrated giant optical activity using a chiral metamaterial composed of an array of conjugated bilayer metal structures. The chiral metamaterials were further integrated with photoactive inclusions to accomplish a wide tuning range of the optical activity through illumination with near-infrared light. The strong chirality observed in our metamaterials results in a negative refractive index, which can also be well controlled by the near-infrared optical excitation.

DOI: [10.1103/PhysRevB.86.035448](https://doi.org/10.1103/PhysRevB.86.035448)

PACS number(s): 78.67.Pt, 81.05.Xj

I. INTRODUCTION

Optical activity, the ability to rotate the polarization plane of electromagnetic waves, occurs in natural chiral materials where molecules lack internal mirror symmetry, such as cholesteric liquid crystals, sugar, and many biomolecules. Despite it being a weak effect, fixed by the molecular structure, optical activity has proven highly important in molecular biology and analytical chemistry.¹ Much stronger optical activity can be created using metamolecules, i.e., resonant chiral elements that underpin the function of metamaterials.² It has been proposed and demonstrated that the optical activity in chiral metamaterials is strong enough to realize a negative index of refraction without the requirements of simultaneous negative permittivity and permeability.^{3–5} Here we experimentally demonstrate chiral metamaterials exhibiting giant optical activity and negative index of refraction in the terahertz regime (1 THz = 10^{12} Hz). More importantly, by integrating semiconducting materials into the metamolecules, optical activity can be dynamically controlled through photoexcitation, without sacrificing transparency or polarization purity. This enables applications for metamaterials in optoelectronics, communications, and imaging when strong control of polarization is desirable or required.

Metamaterials are manmade effective media that can be engineered to exhibit fascinating electromagnetic properties not occurring in nature, such as negative refractive index,^{6–8} “perfect” imaging,^{9,10} and electromagnetic cloaking.^{11,12} Although scalable, the resonant response in metamaterials is typically fixed by their structural geometry and dimensions, which limits their capability in manipulating electromagnetic waves. Metamaterials with dynamically or actively controllable responses have also been demonstrated and expand metamaterial applications to areas such as ultrafast switching,¹³ frequency tuning,¹⁴ amplitude and phase modulation,¹⁵ memory devices,¹⁶ electrochemical switching,¹⁷ and active polarizers.¹⁸ Optical activity in purely chiral (bi-isotropic) media originates from molecular structures that produce magnetic (electric) moments parallel or antiparallel to applied electric (magnetic) fields. Chiral metamolecules are analogously designed to create optical activity in almost any desirable frequency range. By leveraging resonance, metamaterial optical activity is also much stronger and enables giant circular dichroism,¹⁹ negative index of

refraction,^{3–5} and possibly even the reversal of the Casimir force.²⁰ With the subsequent integration of active materials, metamaterial optical activity can be dynamically controlled through the application of an external stimulus.

II. BILAYER CHIRAL METAMATERIAL WITH PURE CHIRALITY

We created dynamically controllable and purely chiral metamaterials consisting of a bilayer conjugated planar metal structure shown in Fig. 1. The conjugated bilayer structure consists of counterfacing gammadion-shaped gold resonators separated by a low-loss polyimide spacer, which is 10 μm thick and is transparent in both the terahertz and near-infrared ranges. The bottom-layer resonators sit on 600-nm-thick square intrinsic silicon islands patterned from a silicon-on-sapphire substrate. The 200-nm-thick gold resonators have a linewidth of 8 μm , and a side length of 60 and 50 μm for top and bottom layers, respectively. The conjugated arrangement of the metallic resonators breaks their mirror symmetry in the direction perpendicular to the plane of the metamaterial, and thereby induces strong chirality around the resonance frequencies. Dynamic tunability in the electromagnetic response is realized through photoexcitation of a thin layer of intrinsic silicon integrated into the chiral metamaterial design.

Surface electric current distributions on metallic structures, shown in Figs. 1(d) and 1(e) and obtained by numerical simulations, elucidate the operational mechanism of the chiral metamaterial. The electric field \mathbf{E} of the incident wave induces circular currents in the U-shaped parts of the resonators [Fig. 1(d)], and results in antiparallel currents (red arrows) in the central parts of the top and bottom resonators due to their conjugated arrangement. A magnetic moment \mathbf{M} , antiparallel to the incident electric field \mathbf{E} , is induced by these antiparallel currents. Similarly, the magnetic field \mathbf{H} of the incident electromagnetic wave induces antiparallel currents [blue arrows in Fig. 1(e)] in the central parts of the resonators resulting in positive and negative charge accumulation in the opposites ends. The time-varying charges generate an electric moment \mathbf{P} parallel to the magnetic field \mathbf{H} . By the aforementioned definition, the fourfold in-plane symmetry results in a pure chiral response.

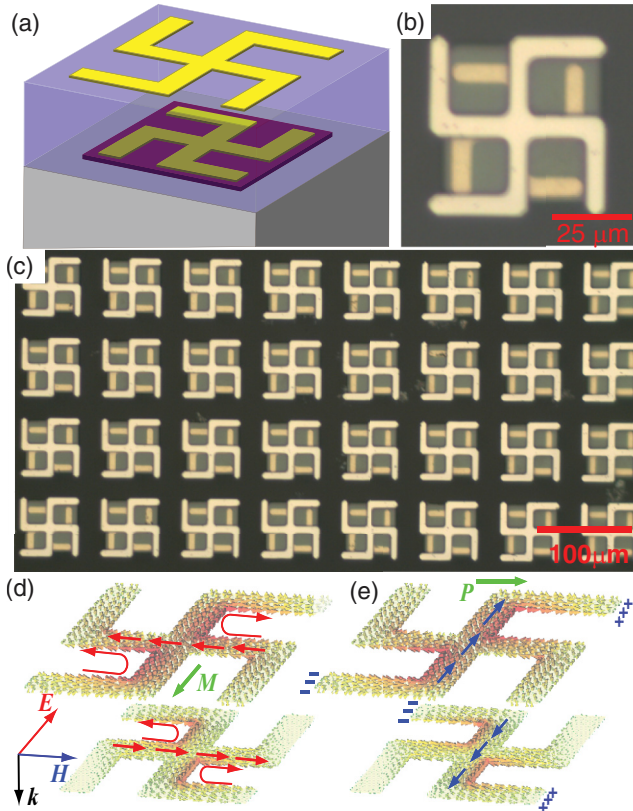


FIG. 1. (Color online) (a) Design schematic of the unit cell of the dynamic chiral metamaterials. Bilayer conjugate gammadion-shaped gold resonators [yellow (light gray)], dielectric spacing layer [blue (dark gray)], and silicon region [red (black)] sit on a dielectric substrate (gray). The microscopic images show (b) a top view of one unit cell and (c) a larger scale of a fabricated sample. The surface current distributions of the chiral metamaterial are obtained from numerical simulations at an off-resonance frequency where strong optical activity still occurs. (d) Magnetic or (e) electric moments are induced by the electric or magnetic fields, respectively, of the incident electromagnetic wave in the antiparallel or parallel direction.

III. TUNABLE OPTICAL ACTIVITY WITH HIGH TRANSMISSION AND LOW POLARIZATION DISTORTION

The frequency response and optical activity of our chiral metamaterials were measured using optical-pump terahertz-probe (OPTP) spectroscopy. Transmission coefficients of circular copolarized [Figs. 2(a) and 2(b)] and cross-polarized fields are determined through linearly polarized measurements (for experimental details see Appendix A). The cross-polarization transmission coefficients (not shown) are nearly zero, indicating circularly polarized waves are the eigenmodes of our metamaterials, and thereby demonstrate pure chirality. We first consider the situation without photoexcitation shown by the red (solid) curves in Fig. 2. Due to the asymmetric geometry, left-handed and right-handed circularly polarized (LCP and RCP) waves reveal different transmission under normal incidence [Figs. 2(a) and 2(b)], which is most prominent at the resonance frequencies of $f_1 = 0.7$ THz and $f_2 =$

1.1 THz. As in typical chiral metamaterials, near the resonance frequencies chirality is maximized by the large magnetic (electric) moments induced by the electric (magnetic) fields, but the transmission is also very low and the polarization distortion is significant, severely limiting its applications.

In order to minimize the polarization distortion and achieve high transmission one can utilize the off-resonance frequency regions of the bilayer chiral metamaterial response. However, rotatory power is usually very weak in these regions^{2,4} and a substantial effort is required to find a chiral metamaterial design with enhanced rotatory power. The conjugated bilayer metallic resonators we employ are one such design. They enable much stronger rotatory power than other chiral metamaterial designs in the off-resonance region between the two resonance modes, as shown in Fig. 2(c). Importantly, in this region low polarization distortion [Fig. 2(d)] and high transmission [Figs. 2(a) and 2(b)] are also evident for both LCP and RCP waves. The rotation angle quantifies the strength of optical activity and is defined by the rotation of the polarization plane as the wave propagates through the chiral metamaterial. For pure chirality, the rotation angle θ is proportional to the chirality parameter κ , or $\theta = \text{Re}\{\kappa\}k_0d = (\phi_{\text{RCP}} - \phi_{\text{LCP}})/2$, where ϕ_{RCP} and ϕ_{LCP} are the phases of the transmission coefficients for RCP and LCP incident waves, and k_0 and d are the wave vector in vacuum and the thickness of the metamaterial, respectively. As shown by the red (solid) curve in Fig. 2(c), the rotation angle is greater than 12° . Ellipticity, defined as $e = (|T_{\text{RCP}}| - |T_{\text{LCP}}|)/(|T_{\text{RCP}}| + |T_{\text{LCP}}|)$, quantifies the polarization state of an electromagnetic wave as the ratio of the semiminor to semimajor axes of the polarization ellipse. The red (solid) curve in Fig. 2(d) illustrates the extremely small ellipticity of the transmitted wave when a linearly polarized (zero ellipticity) incident THz wave propagates through the metamaterial, revealing the unchanged polarization state.

Dynamic control of the chirality is accomplished by exciting photocarriers in the intrinsic silicon islands using near-infrared femtosecond laser pulses. As shown in Fig. 2, the photocarriers increase the silicon conductivity, which dampens the metamaterial resonance. This gradually destroys the induced magnetic (electric) moments, turning the chiral response off. As shown in Fig. 2(c), the rotation angle of the chiral metamaterial can be tuned from 12° to -1° as the laser fluence increases from 0 to $40 \mu\text{J}/\text{mm}^2$, and the ellipticity values in Fig. 2(d) remain less than 0.15. The polarization states of the transmitted waves at 0.85 THz are illustrated in Figs. 2(e)–2(g), where the incident wave is linearly polarized along the horizontal (0°) and the pump laser fluence is 0, 1.5, and $40 \mu\text{J}/\text{mm}^2$. The respective rotation angles are 10.88° , 5.73° , and -0.91° and ellipticities are 0.001, 0.027, and 0.061. The corresponding conductivity in silicon is 0, 5×10^3 , and 5×10^4 S/m, respectively (see details in Appendix B). The chiral response is completely turned off when the laser fluence increases beyond $40 \mu\text{J}/\text{mm}^2$, where a very high conductivity in silicon, 5×10^4 S/m, is achieved. We should point out that such high conductivity requires very high density of free charge carriers in silicon, which is very hard to achieve if one scales down the sizes to make a similar device working at optical frequencies.

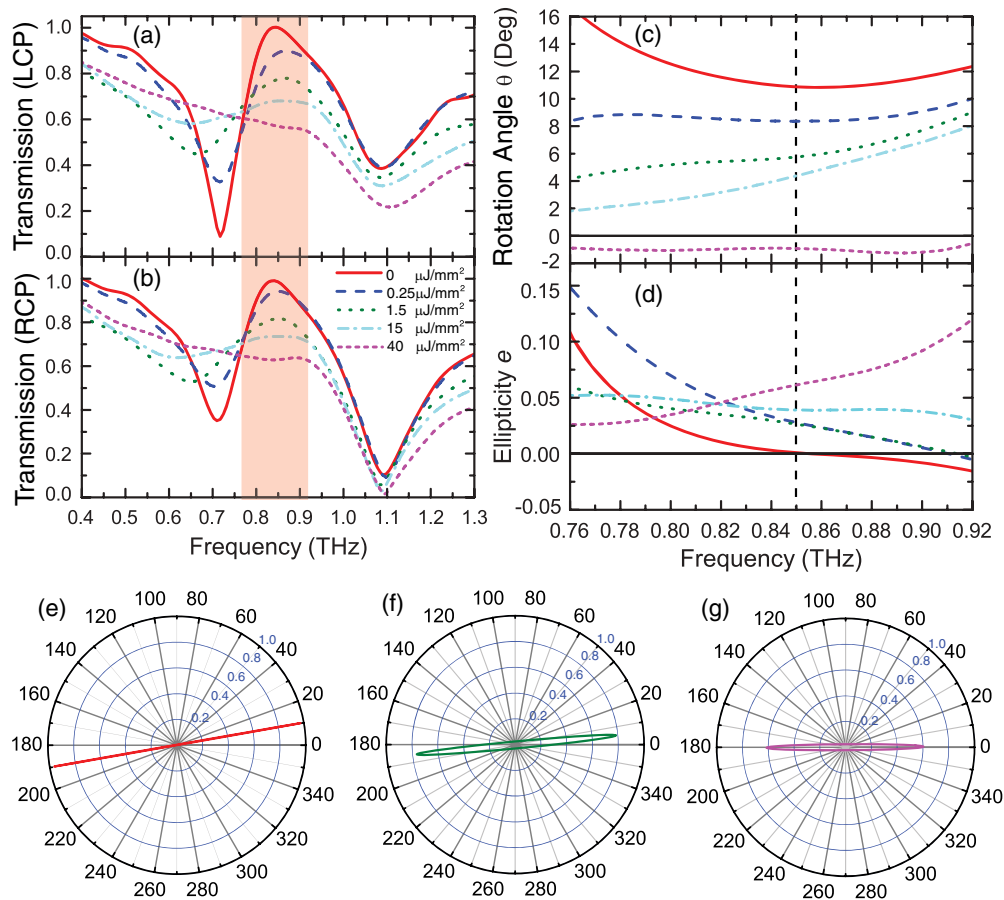


FIG. 2. (Color online) Measured transmission coefficients of (a) left-handed and (b) right-handed circular polarizations (LCP and RCP) under normal incidence at different fluence levels of near-infrared photoexcitation. The shaded region indicates the operation frequency range (off-resonance) with simultaneously high transmission and significant chirality. With linearly polarized incident THz radiation, the (c) rotation angle and (d) ellipticity of the transmission are calculated from the experimental data in (a) and (b). At 0.85 THz, the polar plots show the polarization state of the transmitted wave with photoexcitation fluences of (e) 0, (f) 1.5, and (g) $40 \mu\text{J}/\text{mm}^2$.

IV. TUNABLE NEGATIVE REFRACTIVE INDEX DUE TO CHIRALITY

The metamaterial was further analyzed in terms of effective refractive index and chirality parameters using a retrieval procedure⁴ based on a bi-isotropic model. These effective material parameters may be calculated from measured transmission and reflection coefficients, but the latter were unavailable experimentally. Therefore, finite-element numerical simulations²¹ were utilized after validation with experimental results. Figure 3 shows the refractive index, n_{RCP} and n_{LCP} , and chirality parameter κ for the chiral metamaterial having a silicon island conductivity of $\sigma = 0$ and $5 \times 10^4 \text{ S/m}$, which corresponds to laser fluences of 0 and $40 \mu\text{J}/\text{mm}^2$ (for details see Appendix B). The refractive indices exhibit negative values over different frequency ranges for LCP (green shaded region) and RCP (yellow shaded region) incident waves without photoexcitation. Unlike conventional negative index metamaterials,^{6–8} here the negative index originates from the strong chirality and does not require simultaneous negative permittivity and permeability.^{3–5} For purely chiral materials, the refractive index is $n = \sqrt{\epsilon\mu} \pm \kappa$, where “+” and “–”

refer to the RCP and LCP eigenstates, respectively. As shown in Fig. 3(c), the chirality parameter κ becomes large around the resonance frequencies $f_1 = 0.7 \text{ THz}$ and $f_2 = 1.1 \text{ THz}$, leading to negative values of n_{LCP} and n_{RCP} in the green and yellow shaded regions, respectively. The chirality parameters at the off-resonance frequencies around 0.85 THz are ~ 1.5 , which is enormous compared to natural materials such as quartz,¹ where κ is only 3.9×10^{-5} .

As the silicon conductivity increases, the chirality strength decreases correspondingly, and therefore the refractive index gradually increases from negative to positive values. Blue (dashed) curves in Fig. 3 show the refractive index and chirality parameter when the silicon conductivity is $\sigma = 5 \times 10^4 \text{ S/m}$. The chirality vanishes completely at frequencies below 0.85 THz due to damping in the high-conductivity silicon region. Accordingly, n_{RCP} and n_{LCP} converge within the same frequency range. For frequencies above 0.85 THz, the chirality is also greatly reduced; hence, only a slight difference is observed between the LCP and RCP refractive indices. The photoexcitation also destroys the negative refractive index over the entire frequency range from 0.4 to 1.3 THz.

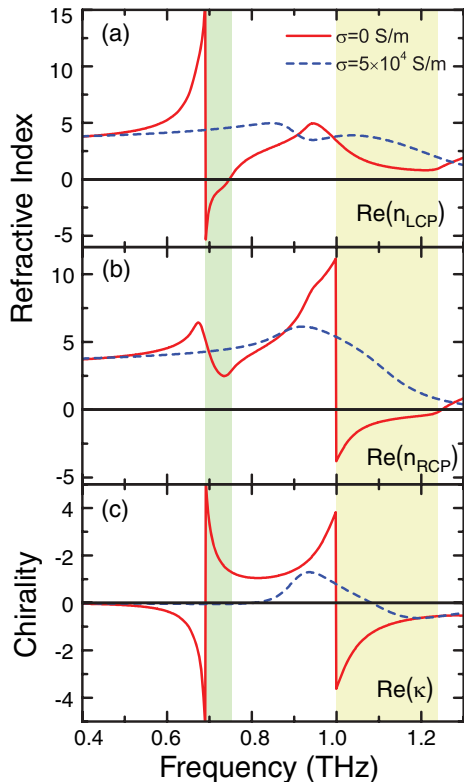


FIG. 3. (Color online) Refractive index for (a) LCP and (b) RCP obtained from numerical simulations with silicon island conductivity $\sigma = 0$ (red solid lines) and 5×10^4 S/m (blue dashed lines), which corresponds to laser fluence of 0 and $40 \mu\text{J}/\text{mm}^2$ in experiments. Green (left) and yellow (right) shaded regions highlight negative values of refractive index, n_{LCP} and n_{RCP} , respectively. (c) Real part of the chirality parameter κ .

V. ENHANCING ROTATORY POWER

The rotatory power in the off-resonance region can be enhanced by changing the relative size of the two resonators. Chirality strength in the off-resonance region [shaded region in Figs. 2(a) and 2(b)] depends on the separation between the two resonance frequencies, f_1 and f_2 . As the two resonances become closer, chirality and optical activity increase significantly. Therefore, the tunable range of chirality can be controlled by changing the metamaterial geometrical dimensions. Decreasing the size of the bottom-layer resonators shifts the low-frequency resonance considerably higher in frequency while leaving the high-frequency resonance unchanged. To demonstrate the enhanced dynamic tunability, we fabricated chiral metamaterials with smaller bottom-layer resonators. Figure 4 shows the rotation angle and ellipticity of these designs. The tuning range of the rotation angle increased to 23° , 28° , and 45° , for bottom-layer resonators with dimensions of 47.5, 45, and $40 \mu\text{m}$, respectively, though ellipticity also increased, altering the polarization state of the transmitted waves as shown.

VI. SUMMARY

Our chiral metamaterials reveal giant optical activity and dynamic tunability with high transmission and very low polar-

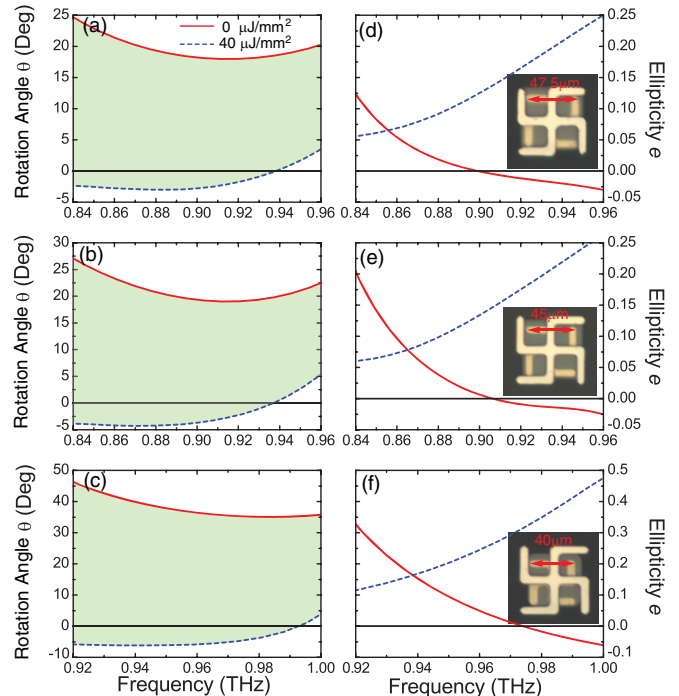


FIG. 4. (Color online) (a)–(c) Measured rotation angle and (d)–(f) ellipticity for dynamic chiral metamaterials with bottom-layer resonator dimensions of 47.5, 45, and $40 \mu\text{m}$, respectively, with the unit cell microscopic images shown in the insets. Size of top-layer resonator is $60 \mu\text{m}$ for all three designs. Red (solid) and blue (dashed) curves show measured rotation angle and ellipticity with the laser fluences of 0 and $40 \mu\text{J}/\text{mm}^2$, respectively. Green shaded regions (a)–(c) show increased tuning range as bottom-layer resonator size decreases.

ization distortion. This is in contrast to previous work achieving a small rotation angle ($\sim 0.5^\circ$) from light-induced optical activity, which was accompanied by polarization distortion and very low transmission.²² Further, our metamaterials demonstrate dynamic control and switching of the negative refractive index. Our metamaterials dramatically advance the state of the art in active chirality, enabling real-world applications such as polarization modulation. These simultaneous advantages in manipulating the polarization of electromagnetic waves will facilitate applications including terahertz optoelectronics, communication, bio-medical microscopy, and imaging.

ACKNOWLEDGMENTS

We acknowledge support from the Los Alamos National Laboratory LDRD Program. This work was performed, in part, at the Center for Integrated Nanotechnologies, a US Department of Energy, Office of Basic Energy Sciences Nanoscale Science Research Center operated jointly by Los Alamos and Sandia National Laboratories. Los Alamos National Laboratory, an affirmative action, equal opportunity employer, is operated by Los Alamos National Security, LLC, for the National Nuclear Security Administration of the US Department of Energy under Contract No. DE-AC52-6NA25396. Work at Ames Laboratory was supported by the Department of Energy (Basic Energy Sciences) under Contract

No. DE-AC02-07CH11358. This was partially supported by the US Office of Naval Research, Award No. N000141010925

APPENDIX A: SAMPLE DESCRIPTION AND MEASUREMENT TECHNIQUE

The dynamic chiral metamaterials were fabricated on a silicon-on-sapphire (SOS) wafer. The wafer has a 600-nm-thick (100) silicon layer grown on a 530- μm -thick *R*-plane (1102) sapphire substrate. The planar silicon and metallic structures were fabricated using standard microfabrication methods. Specifically, the first layer of resonators with side length l_b and linewidth $w = 8 \mu\text{m}$ was fabricated on the surface of the SOS substrate by photolithography, metal deposition (10 nm titanium and 200 nm gold), and lift-off, where l_b is 50, 47.5, 45, and 40 μm for four different samples. The silicon square islands were then defined by photolithography and fabricated by plasma-enhanced etching. A dielectric layer of polyimide with thickness $t_s = 10 \mu\text{m}$ was then spin coated and thermally cured on top of the first metallic and silicon structures. Finally, the second layer of resonators with side length $l_t = 60 \mu\text{m}$ and linewidth $w = 8 \mu\text{m}$ was fabricated on

top of the polyimide using the same methods. The unit cells of our chiral metamaterial were orientated along the primary flat of the sapphire wafer, that is, 45° counterclockwise from the projection of the *C* axis on the *R* plane.

We characterized the dynamic chiral metamaterial using optical-pump terahertz-probe (OPTP) spectroscopy. The transmission of the linearly polarized terahertz pulses through the chiral metamaterial was measured in the time domain, with and without photoexcitation. Photoexcitation utilized near-infrared ($\sim 800 \text{ nm}$) laser pulses ($\sim 50 \text{ fs}$) that illuminated the metamaterial sample a few picoseconds prior to the arrival of the terahertz pulses. The pump laser was focused down to a spot $\sim 5 \text{ mm}$ in diameter on the surface of the chiral sample, exciting electron-hole pairs across the 1.12-eV band gap in all the silicon islands. The power of the laser was varied between 0 and 800 mW corresponding to a fluence on the sample between 0 and 40 $\mu\text{J}/\text{mm}^2$. To obtain the transmission coefficients of circularly polarized waves, i.e., T_{++} , T_{-+} , T_{+-} , and T_{--} , we measured four linear copolarization and cross-polarization transmission coefficients, T_{xx} , T_{yx} , T_{xy} , and T_{yy} . Transmission coefficients of circularly polarized waves were then obtained from the linear measurements using the following equation:

$$\begin{pmatrix} T_{++} & T_{+-} \\ T_{-+} & T_{--} \end{pmatrix} = \frac{1}{2} \begin{bmatrix} (T_{xx} + T_{yy}) + i(T_{xy} - T_{yx}) & (T_{xx} - T_{yy}) - i(T_{xy} + T_{yx}) \\ (T_{xx} - T_{yy}) + i(T_{xy} + T_{yx}) & (T_{xx} + T_{yy}) - i(T_{xy} - T_{yx}) \end{bmatrix}, \quad (\text{A1})$$

where the first and second subscripts refer to the incident and transmitted wave, “+” and “-” refer to the right-handed and left-handed circularly polarized waves, and “x” and “y” refer to the two linearly polarized waves with the electric field polarized along two orthogonal directions. Figure 5 shows the details of our measurement setup, where a pair of THz wire-grid polarizers were used to define two orthogonal directions. As the polarization of the first polarizer P_1 was oriented 45° degree from horizontal, T_{xx} and T_{yx} were measured with the second polarizer P_2 oriented 45° and 135°, respectively. Similarly, T_{xy} and T_{yy} were measured with P_1 oriented 135°

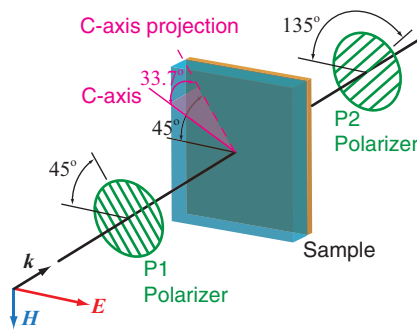


FIG. 5. (Color online) Measurement setup for chiral metamaterials. One THz wire-grid polarizer was installed ahead of and one behind the sample, each oriented either 45° or 135° with respect to the horizontal. The THz electromagnetic wave was polarized horizontally and was incident from the substrate (sapphire) side [blue region (light gray)] of the samples.

and P_2 oriented 45° and 135°, respectively. Since the *R*-plane sapphire substrate is uniaxial with the optical axis (*C* axis) oriented 33.7° with respect to the plane of the substrate (Fig. 5), the metamaterial sample must be oriented during fabrication and measurements to ensure the terahertz wave polarization does not rotate as it propagates through the sapphire substrate. During our measurements, the orientation of the metamaterial sample was carefully set so that the projection of the *C* axis on the *R* plane was parallel to the 45° direction. The terahertz wave polarization is set by the polarizer P_1 ; the electric field is either parallel (P_1 oriented 45°) or perpendicular (P_1 oriented

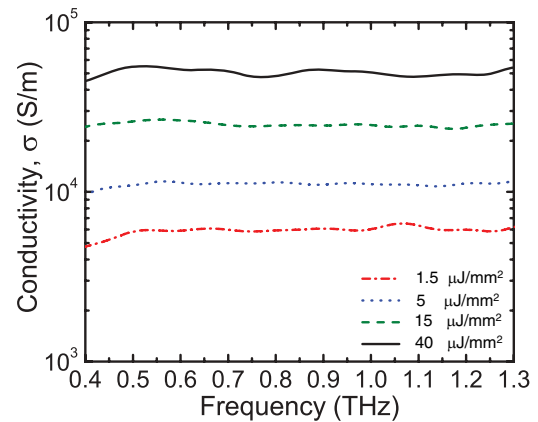


FIG. 6. (Color online) Measured conductivity of the silicon layer on the sapphire substrate for laser fluences of 1.5, 5, 15, and 40 $\mu\text{J}/\text{mm}^2$.

135°) to the projection of the C axis. Therefore, the terahertz wave retains its linear polarization state without suffering any rotation as it propagates through the sapphire.

APPENDIX B: CONDUCTIVITY OF SILICON UNDER LASER ILLUMINATION

As shown in Fig. 6, the conductivity of the silicon layer was measured under different illumination intensities. Specifically, the transmission coefficients, T_{SOS} , through the unpatterned SOS wafer were measured using the OPTP

system. The transmission coefficient of the silicon layer was then obtained using $T_{\text{Si}} = T_{\text{SOS}}/T_{\text{Sub}}$, where T_{Sub} is the transmission coefficient of the sapphire substrate calculated by its measured refractive index and known thickness. By using a fitting procedure, we calculated the conductivity of the silicon layer from the transmission coefficient T_{Si} . Figure 6 shows that the photoexcited conductivities of the silicon layer are nearly constant between 0.4 and 1.3 THz. The corresponding conductivities for pump laser fluences of 1.5, 5, 15, and 40 $\mu\text{J}/\text{mm}^2$ are 5×10^3 , 1×10^4 , 2.5×10^4 , and 5×10^4 S/m, respectively.

*Present address: Department of Physics, University of South Florida, Tampa, Florida, 33620; jiangfengz@usf.edu

†H.-T. Chen (chenht@lanl.gov)

‡Present address: Department of Electrical and Computer Engineering, Oklahoma State University, Stillwater, Oklahoma, 74078; oharaj@okstate.edu

¹I. V. Lindell, A. H. Sihvola, S. A. Tretyakov, and A. J. Viitanen, *Electromagnetic Waves in Chiral and Bi-isotropic Media* (Artech House, Boston, London, 1994).

²A. V. Rogacheva, V. A. Fedotov, A. S. Schwanecke, and N. I. Zheludev, *Phys. Rev. Lett.* **97**, 177401 (2006).

³J. B. Pendry, *Science* **306**, 1353 (2004).

⁴E. Plum, J. Zhou, J. Dong, V. A. Fedotov, T. Koschny, C. M. Soukoulis, and N. I. Zheludev, *Phys. Rev. B* **79**, 035407 (2009).

⁵S. Zhang, Y. S. Park, J. Li, X. Lu, W. Zhang, and X. Zhang, *Phys. Rev. Lett.* **102**, 023901 (2009).

⁶R. Shelby, D. Smith, and S. Schultz, *Science* **292**, 77 (2001).

⁷C. M. Soukoulis, S. Linden, and M. Wegener, *Science* **315**, 47 (2007).

⁸V. M. Shalaev, *Nat. Photonics* **1**, 41 (2007).

⁹J. B. Pendry, *Phys. Rev. Lett.* **85**, 3966 (2000).

¹⁰N. Fang, H. Lee, C. Sun, and X. Zhang, *Science* **308**, 534 (2005).

¹¹J. B. Pendry, D. Schurig, and D. R. Smith, *Science* **312**, 1780 (2006).

¹²D. Schurig, J. J. Mock, B. J. Justice, S. A. Cummer, J. B. Pendry, A. F. Starr, and D. R. Smith, *Science* **314**, 977 (2006).

¹³W. J. Padilla, A. J. Taylor, C. Highstrete, M. Lee, and R. D. Averitt, *Phys. Rev. Lett.* **96**, 107401 (2006).

¹⁴H.-T. Chen, J. F. O'Hara, A. K. Azad, A. J. Taylor, R. D. Averitt, D. B. Shrekenhamer, and W. J. Padilla, *Nat. Photonics* **2**, 295 (2008).

¹⁵H.-T. Chen, W. J. Padilla, M. J. Cich, A. K. Azad, R. D. Averitt, and A. J. Taylor, *Nat. Photonics* **3**, 148 (2009).

¹⁶T. Driscoll, H.-T. Kim, B.-G. Chae, B.-J. Kim, Y.-W. Lee, N. M. Jokerst, S. Palit, D. R. Smith, M. Di Ventra, and D. N. Basov, *Science* **325**, 1518 (2009).

¹⁷Y. Leroux, J. C. Lacroix, C. Fave, G. Trippe, N. Félidj, J. Aubard, A. Hohenau, and J. R. Krenn, *ACS Nano* **2**, 728 (2009).

¹⁸Y. Leroux, J. C. Lacroix, C. Fave, V. Stockhausen, N. Félidj, J. Grand, A. Hohenau, and J. R. Krenn, *Nano Lett.* **9**, 2144 (2009).

¹⁹J. K. Gansel, M. Thiel, M. S. Rill, M. Decker, K. Bade, V. Saile, G. von Freymann, S. Linden, and M. Wegener, *Science* **325**, 1513 (2009).

²⁰R. Zhao, J. Zhou, T. Koschny, E. N. Economou, and C. M. Soukoulis, *Phys. Rev. Lett.* **103**, 103602 (2009).

²¹Computer Simulation Technology GmbH, Darmstadt, Germany.

²²N. Kanda, K. Konishi, and M. Kuwata-Gonokami, *Opt. Lett.* **34**, 3000 (2009).